Interfaces of dicationic ionic liquids and graphene: a molecular dynamics simulation study

2014 J. Phys.: Condens. Matter 26 284106

(http://iopscience.iop.org/0953-8984/26/28/284106)

IOP Publishing Journal of Physics: Condensed Matter
J. Phys.: Condens. Matter **26** (2014) 284106 (11pp) doi:10.1088/0953-8984/26/28/284106

Interfaces of dicationic ionic liquids and graphene: a molecular dynamics simulation study

Song Li[1], **Guang Feng**[1,2], **and Peter T Cummings**[1]

[1] Department of Chemical and Biomolecular Engineering, Vanderbilt University, Nashville, TN 37235, USA
[2] State Key Laboratory of Coal Combustion, Huazhong University of Science and Technology, Wuhan 430074, People's Republic of China

E-mail: guang.feng@vanderbilt.edu

Received 20 November 2013, revised 21 January 2014
Accepted for publication 10 February 2014
Published 12 June 2014

Abstract
Molecular dynamics simulations were performed to investigate the interfacial structure and capacitance of electrical double layers (EDLs) in dicationic ionic liquids (DILs) 1-alkyl-3-dimethylimidazolium tetrafluoroborate $[C_n(mim)_2](BF_4)_2$ (n = 3, 6, 9), with respect to a baseline of a monocationic ionic liquid $[C_3mim][BF_4]$, near planar carbon electrodes consisting of graphene sheets. The simulation results show that an adsorbed layer with double peaks is exclusively found for $[C_3(mim)_2](BF_4)_2$, while a single peak of the other three cations is observed at the neutral electrode, due to the difference in ion–wall interaction and cation–anion association. As the electrode becomes negatively charged, the second peak of $[C_3(mim)_2]^{2+}$ is dramatically reduced, whereas those of $[C_6(mim)_2]^{2+}$ and $[C_9(mim)_2]^{2+}$ become non-trivial. The capacitance–potential curve of EDLs in DILs manifests a transition from camel shape to bell shape as the cation chain length increases, which is attributed to the enlargement of ion adsorption (per unit charge) on the electrode and the decrease of attractive interaction between ions.

Keywords: dicationic ionic liquid, electrical double layer, interfacial structure, differential capacitance, graphene, supercapacitor

S Online supplementary data available from stacks.iop.org/J.Phys/26/284106/mmedia

(Some figures may appear in colour only in the online journal)

1. Introduction

Electrical energy generated from renewable energy sources, such as solar and wind, renders a great potential for meeting future energy demands with respect to the sharp increase in world energy use over the past decades [1, 2]. However, the use of electricity from intermittent sources requires efficient electrical energy storage (EES). Thanks to their advantageous properties such as high power density, high capacitance and excellent performance stability, electrical double-layer capacitors (EDLCs), also named supercapacitors or ultracapacitors, storing electrical energy physically in double layers, have emerged as a promising type of EES device in recent years [3–5]. Due to their high power-handling ability superior to that of batteries, supercapacitors are particularly in demand for applications requiring energy delivered in a short time; e.g. electric vehicles, buses, cranes, forklifts, wind turbines and in opening emergency doors of airplanes [1, 7, 8]. However, the primary limitation of supercapacitors is their moderate energy density compared to batteries [5, 8]. The energy density, E, is related to the capacitance, C, and the device operating voltage, V; i.e. $E = C{\cdot}V^2/2$ [4]. Thus, the approach of enhancing supercapacitors' energy density is to increase the maximum operating voltage and/or to optimize their charge storage capacity by enlarging the electrode surface area.

Achieving a fairly high operating voltage (4–6 V; e.g. ~4.0 V for protic ionic liquids (ILs) [9], ~4.5 V for imidazolium ILs [10] and ~5.5 V for pyrrolidinium and tetraalkylammonium

ILs [11, 12]) in contrast to aqueous and organic electrolytes, ILs have become a very advanced class of electrolytes for supercapacitors, also benefiting from other advanced properties including excellent thermal stability, non-volatility and a relatively inert nature [13, 14]. The structures of electrical double layers (EDLs) at interfaces of ILs and electrified surfaces have been widely studied by experimental, theoretical and modeling methods. In a high-energy x-ray reflectivity study on the temperature-dependent structures of ILs at a charged sapphire substrate, Mezger *et al* [15] suggested that the layering of cations and anions is a generic feature of interfacial ILs, which was in agreement with the oscillation in the ion density predicted by molecular dynamics (MD) simulations [16–18] of ILs modeled by a united atom model and confined between two flat parallel walls. Using MD simulations with ILs in an all-atom model [19–21], it was further confirmed that due to the strong cation–anion correlations, the ion layering in ILs near the electrode surface is about 1.5–3.0 nm in thickness. Specific imidazolium-based cations, despite different chain lengths, were found to adsorb significantly on neutral and negatively charged electrodes, and the imidazolium ring becomes more parallel to the electrode surface as the electrode charge density, σ, becomes more negative, and tends to be more vertical to the electrode surface as σ becomes more positive [18, 19, 22–24]. Using surface force apparatus, Perkin *et al* [25–28] investigated the IL structure between two atomically smooth negatively charged surfaces and classified the different ion layerings into two categories: short-chain cation ILs form alternating cation–anion monolayers while ILs with long-chain cations result in the formation of bilayers.

In addition to the interfacial structure, the most extensively studied macroscopic property of EDLs in ILs is the curve between the differential capacitance and electrode potential (i.e. the *C–V* curve [29, 30]). Different varieties of *C–V* curves have been observed experimentally and predicted computationally, including the U-shaped, bell-shaped and camel-shaped types for supercapacitors with planar electrodes, indicating that the differential capacitance is intimately associated with the electrode potential [29–33]. The chain length of cations was found to play an important role in the *C–V* curve, and suggested by both experiment [30, 34–39] and modeling [40, 41]. The overall differential capacitance is observed to decrease with the increase of the chain length due to the thicker EDL formed by large cations [30, 36], although experimental measurements showed that the *C–V* curve relies on the electrode materials [30], ion types [30, 42], temperature [30, 36, 38] and ion size [30, 36, 38]. Interestingly, a Monte Carlo simulation reported that the *C–V* curve transitioned from the bell to the camel shape with the increase of the alkyl chain in the cation at the graphite electrode [40], while an MD simulation study [41] showed that the camel-shaped *C–V* curve near planar graphite-based electrodes tends to be less evident. Unlike any aforementioned *C–V* curves, our recent MD work on ILs on nano-scale curved surfaces (onion-like carbon and carbon nanotube electrodes) showed that the differential capacitance depends weakly on the electrode voltage; i.e. the *C–V* curve is nearly flat in contrast to that at the planar electrode surface [43].

However, these above observations/results are focused on monocationic ILs (MILs), i.e. with monovalent cations. To expand the diversity of the cation family, a series of imidazolium- and pyrrolidinium-based geminal dicationic ILs (DILs) were developed with two identical imidazolium or pyrrolidinium rings bridged by alkyl chains, which could achieve higher stability than MILs [44–46]. To date, the work on interfaces of DILs and solid surfaces is quite elusive, and efforts are needed to answer the question of whether the aforementioned conclusions are still tenable when replacing MILs with DILs, and, most importantly, how the EDL structure and *C–V* curve are changed.

Motivated by these considerations, in this work, we performed MD simulations to model DILs, 1-alkyl-3-dimethylimidazolium tetrafluoroborate $[C_n(mim)_2](BF_4)_2$ (n = 3, 6, 9), with respect to a baseline of an MIL of $[C_3mim][BF_4]$ in contact with planar carbon electrodes composed of graphene sheets under a series of applied potentials. Our simulations show that the layering of cations/anions is still a key feature for EDLs in DILs near planar carbon electrodes; however, a different structure of the adsorbed ion layer was observed for short-chain DILs. With increasing chain length, the camel-shaped *C–V* curve was found to be less defined (and tended to be bell-shaped). The rest of the paper is organized as follows: section 2 presents the simulation method and models; section 3 shows the structure of ILs near neutral/charged planar carbon electrodes; the potential of zero charge (PZC) of different ILs and the EDL capacitance are shown and discussed in section 4; finally, conclusions are drawn in section 5.

2. Simulation method and models

Figure 1(*a*) shows the molecular structure of ions in DILs $[C_n(mim)_2](BF_4)_2$ (n = 3, 6, 9) and MIL $[C_3mim][BF_4]$ studied in this work. The simulation system, as a channel shown in figure 1(*b*), consisted of a slab of electrolytes enclosed between two electrodes, and each electrode was modeled as three-layered graphene sheets with a gap of 0.34 nm between each two neighboring sheets. The separation between the two electrodes was set to 8.0 nm (the distance between the innermost layers of opposing channel walls) to reproduce a bulk-state behavior of ILs in the channel center. To generate the different applied potentials, the partial charge was uniformly distributed among the carbon atoms on the innermost layers of the electrodes, and the two innermost layers carry the same surface charge with opposite signs to keep the neutrality of the simulation system. It is worthwhile noting that the constant potential method could be enhanced for treating the particular case of carbon materials (e.g. porous carbons [47, 48]), since the image charge effects [49–52] induced by the electrode were considered. However, when the electrode surface is flat (e.g. planar graphene) and ILs are used as the electrolyte [53], under a potential within about −3 to 3 V, ion density profiles are almost the same for simulations using the constant potential assembly and the constant charge surface [53]. Thus, taking into account the potential range of −2.6 to 3.1 V and the all-atom model used in this work, it is applicable to use the

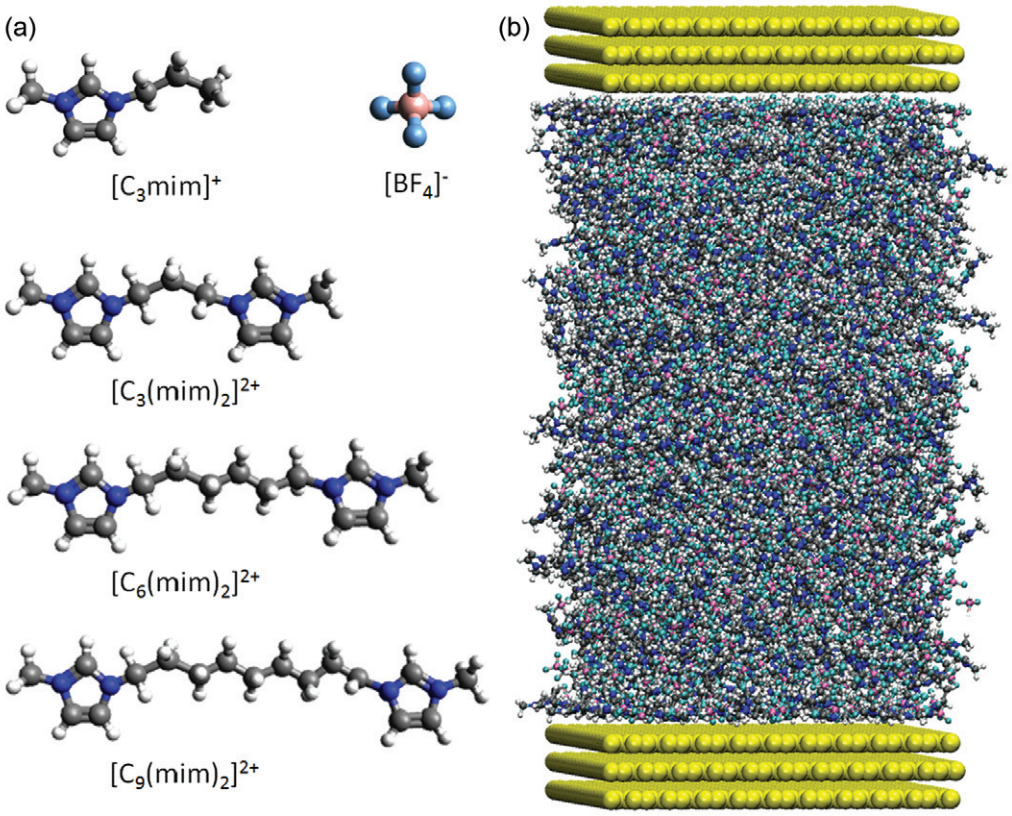

Figure 1. (*a*) Molecular structure of monocations, dications and anions in ILs used in this study. (*b*) Snapshot of MD simulation system, in which the yellow spheres represent the graphite electrodes and ILs were enclosed between the two electrodes.

constant surface charge assembly to model the interfaces of ILs and planar graphene.

Due to the high melting point (>390 K [45]) of the studied DILs that can be used in high-temperature supercapacitors [54], to ensure that all ILs were in liquid phase, all the simulations were performed at 450 K, the same temperature as used in a previous MD study by another group [55]. MD simulations were performed in the NVT ensemble using a user-modified version of the MD package GROMACS [56]. The force field used for DILs $[C_n(mim)_2](BF_4)_2$ (n = 3, 6, 9) was taken from the MD work by Yeganegi *et al* [55], which has been validated and used to predict the densities of DILs with high accuracy compared with experimental data [45]. The force field for MIL $[C_3mim][BF_4]$ was taken from the study by Lopes' group [57]. The van der Waals interaction parameters for carbon of the graphite electrode were taken from the work of Cornell *et al* [58].

In the simulation system, the electrolyte temperature was maintained at a setting value using the Berendsen thermostat. The slab-PME method [59] was used to compute the electrostatic interactions in the two-dimensionally periodic geometry adopted here. Specifically, the dimension vertical to the electrode of the simulation box was set to be five times the electrode separation [60], which is sufficient to ensure that the accuracy of the electrostatic force calculation is comparable to that of the two-dimensional Ewald method [59]. An FFT grid spacing of 0.10 nm and cubic interpolation for charge distribution were used to compute the electrostatic interactions in reciprocal space. A cutoff distance of 1.1 nm was used in the calculation of electrostatic interactions in real space. All the C–H bonds were constrained using the LINCS algorithm [61] during the simulation and a 1.1 nm cutoff was used for van der Waals interactions. Each simulation was started at 1000 K and subsequently annealed gradually to 450 K in 9 ns. Following annealing, the system was simulated at that temperature for another 9 ns to reach equilibrium. Finally, a 20 ns production run was performed for analysis. To ensure the accuracy of the simulation results, each system was repeated three times with different initial configurations.

We computed the ion/charge distributions in the direction perpendicular to the electrode surface, using the binning method [62] to analyze the data from MD trajectories and obtain details of the EDL structure. Taking the direction perpendicular to the electrode surface as the z-direction, the potential distribution across an EDL was computed by solving the Poisson equation with two boundary conditions: $\phi(0) = 0$ at the electrode surface and $\mathrm{d}\phi/\mathrm{d}z = 0$ in the middle portion between electrodes; that is,

$$\phi(z) = -\frac{1}{\varepsilon_0}\int_0^z (z-u)\rho_e(u)\,\mathrm{d}u - \frac{\sigma}{\varepsilon_0}z. \qquad (1)$$

Knowing ρ_e, the charge density across EDL, one can obtain the potential drop, ϕ_{EDL}, between the electrode surface and the channel center, and then calculate the differential capacitance by $C = \mathrm{d}\sigma/\mathrm{d}\phi$. In this work, the potential at the central part of the channel was obtained by averaging the potential distribution profile within the region of 3–5 nm from the electrode surface, since ILs in such regions show bulk-state behavior,

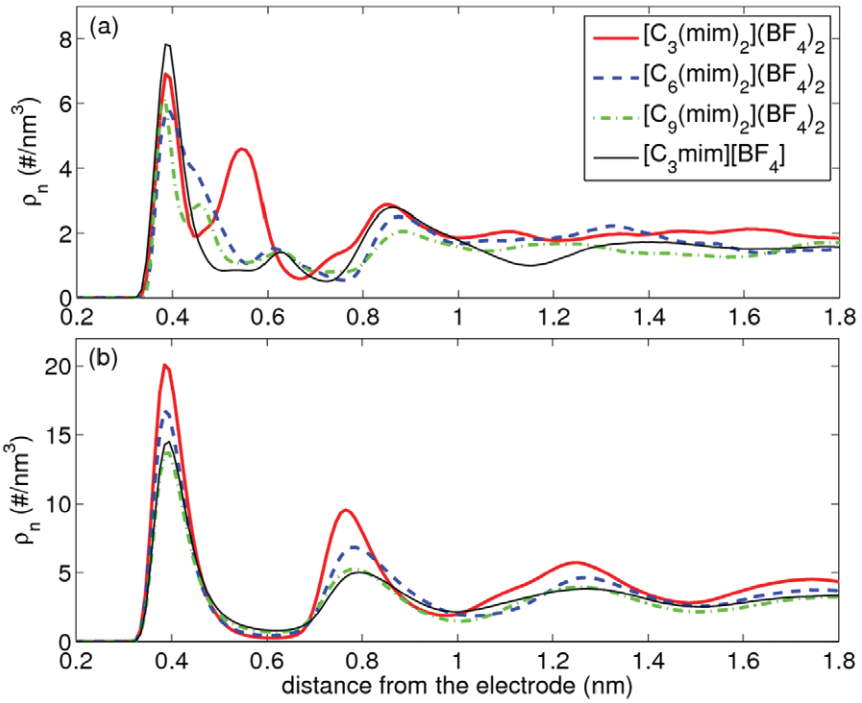

Figure 2. Cation (*a*) and anion (*b*) number density profiles in DILs $[C_3(mim)_2](BF_4)_2$, $[C_6(mim)_2](BF_4)_2$, $[C_9(mim)_2](BF_4)_2$ and MIL $[C_3mim][BF_4]$ near neutral planar carbon electrodes. The positions of the cation and the anion are represented by their center of mass. The number density profile for monocation $[C_3mim]^+$ in (*a*) was scaled by $\frac{1}{2}$.

and the charge density as well as the potential distribution profiles have little fluctuation.

3. Structure of interfacial ILs

Structure of DILs near neutral electrodes. Figure 2 shows the ion distribution described by ion number density profiles, ρ_n, in DILs $[C_3(mim)_2](BF_4)_2$, $[C_6(mim)_2](BF_4)_2$ and $[C_9(mim)_2](BF_4)_2$, as well as MIL $[C_3mim][BF_4]$ near the neutral carbon electrode. Throughout this work, the number density of ions in the channel simulation system was computed based on the center of mass of the ions. An adsorbed layer was observed for both cation and anion. However, the short-chain DIL $[C_3(mim)_2](BF_4)_2$ exhibits a cation layer with double peaks located at 0.38 nm and 0.55 nm, respectively, whereas the other three ILs have a similar cation layer with one peak at about 0.38 nm; there is a single anion peak for all studied ILs and the ion peak height ratio of cation : anion is close to 1 : 1 for the MIL and 1 : 2 for the DILs, with the exception of $[C_3(mim)_2](BF_4)_2$ due to the double peaks of $[C_3(mim)_2]^{2+}$ decreasing the first ion peak. The feature of adsorbed layers agrees with previous observations of imidazolium-based monocations accumulating on the electrode [18, 19, 22, 23, 63] due to the strong interaction between the cation and electrode. We also computed the interaction potential energy between ions and the neutral planar carbon electrode by first taking the sum of the interaction potential between each atom of an ion and carbon atoms of the electrode and then averaging the potential energy of the same type of ions that have different conformations but are at the same distance from the electrode surface. As shown in figure 3, the

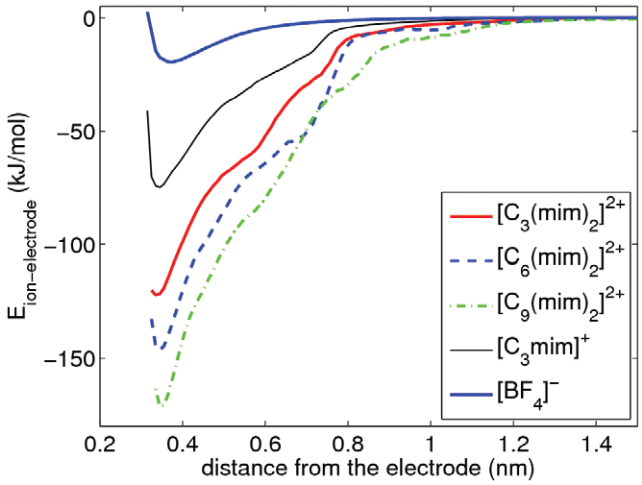

Figure 3. Interaction potential energy between ions and the neutral planar carbon electrode as a function of distance from the electrode.

interaction between dication and electrode increases with the cation chain length and the maximum interaction potential (absolute value) for dication $[C_6(mim)_2]^{2+}$ is nearly two times that for monocation $[C_3mim]^+$, but those for all cations are much larger than that of the anion $[BF_4]^-$. Determined from Molinspiration software[3], the volume of $[C_3(mim)_2]^{2+}$, $[C_6(mim)_2]^{2+}$, $[C_9(mim)_2]^{2+}$, $[C_3mim]^+$ and $[BF_4]^-$ ions was

[3] Molinspiration Interactive Property Calculator, www.molinspiration.com (accessed November 2011). The calculation of molecule volume in Molinspiration software is based on group contributions, by fitting sum of fragment contributions to 'real' 3D volume for a training set of about 12 000, with help of the semiempirical AM1 method (i.e. a generalization of the modified neglect of differential diatomic overlap approximation).

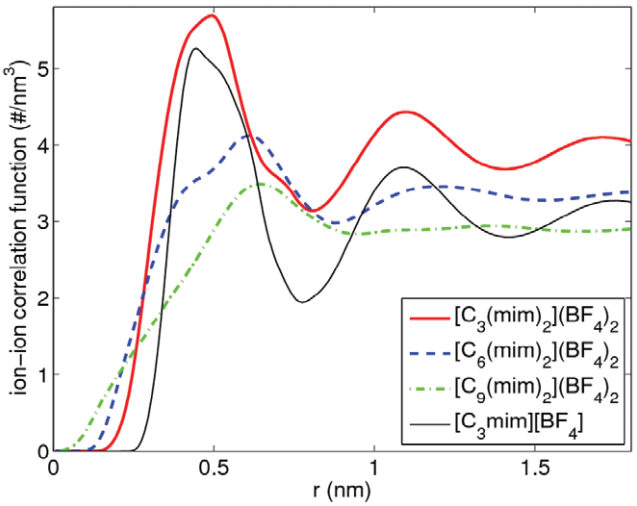

Figure 4. Cation–anion center-of-mass correlation functions as obtained from MD simulations at 450 K.

found to be 0.2079 nm^3, 0.2583 nm^3, 0.3087 nm^3, 0.1352 nm^3 and 0.0732 nm^3, respectively. The trend in ion volume follows that of the ion–electrode interaction potential, which could indicate that the first cation peak at the neutral electrode is under a competitive influence whereby the strong adsorption facilitates the ion packing while the large ion volume restricts the packed ion number on graphene surfaces [25, 27].

However, it is not clear why there is a layer with double peaks for dication $[C_3(mim)_2]^{2+}$. To answer this question, we dissected the cation–anion correlation function shown in figure 4 by computing the anion number density in the radial direction of the cation. It can be seen that the short-chain dications ($[C_3(mim)_2]^{2+}$) have stronger association with the $[BF_4]^-$ ion than the longer chain cations ($[C_6(mim)_2]^{2+}$ and $[C_9(mim)_2]^{2+}$), characterized by a much higher intensity of the first peak for cation–anion correlation. Furthermore, dication $[C_3(mim)_2]^{2+}$ renders a stronger ion coupling with $[BF_4]^-$ than monocation $[C_3mim]^+$ due to the greater charge carried in the former, verified by the higher and wider first peak (figure 4). Therefore, when adsorbed on a neutral surface, the dication $[C_3(mim)_2]^{2+}$ could cause more anions to accumulate on the surface regardless of the weak adsorption of anions toward the electrode surface, which results in the higher anion peaks located at 0.38 and 0.76 nm. Previous MD simulations have revealed that the anions most likely cluster around the rings of a dication [64]. Thus, some $[C_3(mim)_2]^{2+}$ dications could be tilted to leave a space for anions tightly associating with the positively charged ring, which leads to the presence of the second peak of the adsorbed dication layer on the electrode surface; while monocation $[C_3mim]^+$ can relatively easily tilt its tail for anion packing. This can be evidenced by cation orientation discussed below.

Figure 5 shows the orientation of cations near the neutral electrode by computing the order parameter of the ions; i.e. $P_2(\cos\theta) = \langle(3\cos^2\theta-1)/2\rangle$. In figure 5(*a*), θ is defined as the angle formed by the normal vector of the electrode and the normal vector of the imidazolium ring of the cation (one ring was used for orientation calculation due to the symmetry of dication), and θ in figure 5(*b*) is defined as the angle formed by the normal vector of the electrode and the vector through the alkyl chain of the cation. Note that within ~0.48–0.8 nm from the electrode surface (figure 2), with the exception of $[C_3(mim)_2]^{2+}$, there are very few cations. We observe that (1) the ring of the cation in the first adsorbed peak tends to be parallel to the surface and is more tilted as it moves further away from the surface; (2) the alkyl chain of the cation is most parallel to the surface, with the exception of monocation $[C_3mim]^+$ which shows a clear tilted tail; (3) the dication $[C_3(mim)_2]^{2+}$ in the second peak of the adsorbed layer is more tilted than that in the first peak; (4) the orientational ordering parameter approaches zero beyond a position of about 1.5 nm from the electrode, similar to the layering depicted by ion number density profiles in figure 2, which is in line with previous modeling work on MILs [20–22, 63, 65]. These observations, together with the structure described in figure 2, suggest that the double-peaked adsorbed layer for dication $[C_3(mim)_2]^{2+}$ and the one-peaked layer for the other cations are essentially determined by the ion size, ion–electrode interaction and cation–anion association.

Structure of DILs near charged carbon electrodes. Figure 6 exhibits the number density profiles of ions in DILs $[C_3(mim)_2](BF_4)_2$, $[C_6(mim)_2](BF_4)_2$ and $[C_9(mim)_2](BF_4)_2$ as well as MIL $[C_3mim][BF_4]$ near negatively charged electrodes with a surface charge density $\sigma = -0.10\,C\,m^{-2}$ and positive electrodes with $\sigma = +0.10\,C\,m^{-2}$. It is observed that there is a distinct peak of counter-ions accumulating at the charged surface: the peak location is about 0.37 nm for cations and 0.355 nm for anion $[BF_4]^-$; meanwhile, the co-ions become further away from the surface due to the repulsive electrostatic force from charged electrodes. These observations are consistent with simulation work on different imidazolium-based MILs in literature [20–22, 63, 65, 66]. The peak of the first anion layer in all DILs and MILs is very similar (in location, height and width) near the positively charged electrodes. However, there are some distinctions of cations near the negatively charged electrodes: (i) the peak location is 0.355 nm, 0.365 nm, 0.375 nm and 0.375 nm for $[C_3(mim)_2]^{2+}$, $[C_6(mim)_2]^{2+}$, $[C_9(mim)_2]^{2+}$ and $[C_3mim]^+$, respectively; (ii) as the electrode surface charge increases from 0 to $-0.10\,C\,m^{-2}$, the second peak of dication $[C_3(mim)_2]^{2+}$, located at about 0.56 nm, is dramatically decreased, whereas those of $[C_6(mim)_2]^{2+}$ and $[C_9(mim)_2]^{2+}$ become non-trivial; (iii) there is a near depletion for monocation $[C_3mim]^+$ within ~0.48–0.8 nm. The orientation of cations near the negatively charged electrode, shown in Figure S1 of the online supporting information (stacks.iop.org/J.Phys/26/284106/mmedia), indicates that the cation rings in the adsorbed layer become more parallel to the electrode surface. The chain of dication also tends to be more parallel to the surface due to the orientation change of its two rings, while the chain of monocation $[C_3mim]^+$ seems to exhibit little variation. This may be ascribed to the fact that the linked chain in dications has more constraints than the free tail in the monocation.

Although the different structure of the adsorbed layer of DILs with different chain lengths as well as the MILs observed in this work is mainly found for short-chain DILs, more discrepancies may be revealed for the long-chain DILs versus MILs, which will be included in our future work, especially for the interfaces of ILs and other solid substrates (e.g. mica with intrinsic partial charges among surface atoms).

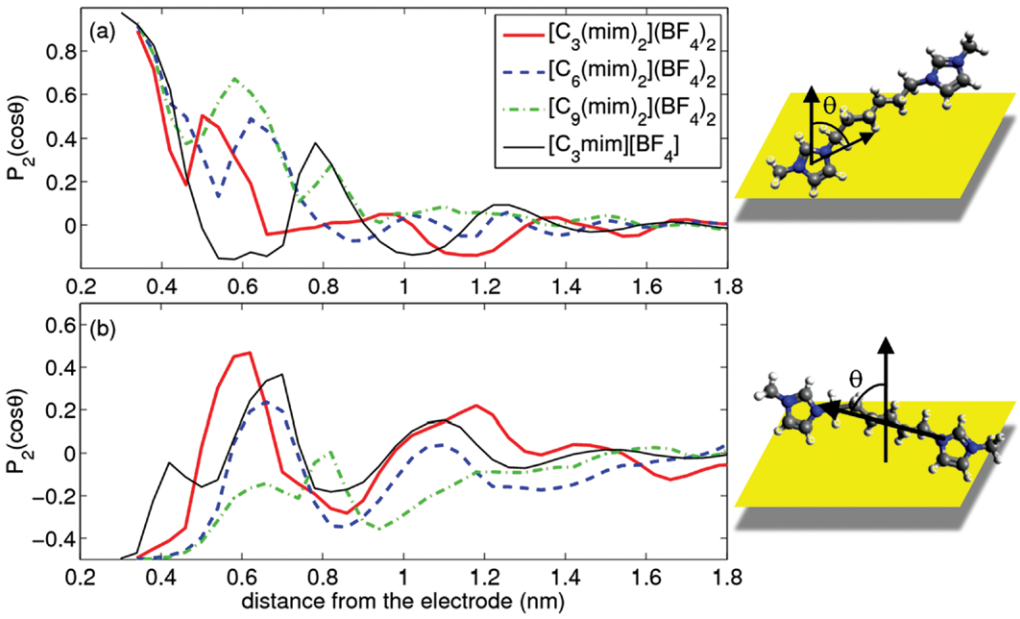

Figure 5. Orientational order parameter $P_2(\cos\theta)$ of cation ring (*a*) and cation chain (*b*) in DILs $[C_3(mim)_2](BF_4)_2$, $[C_6(mim)_2](BF_4)_2$, $[C_9(mim)_2](BF_4)_2$ and MIL $[C_3mim][BF_4]$ near neutral planar carbon electrodes.

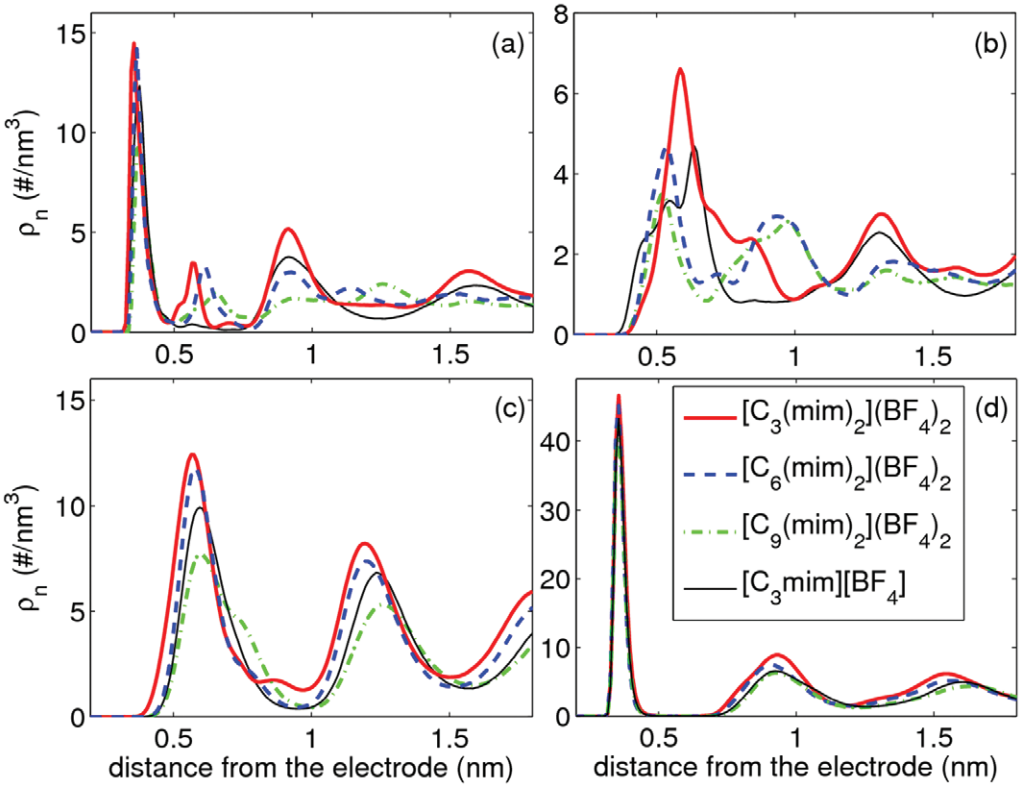

Figure 6. Cation (*a*), (*b*) and anion (*c*), (*d*) number density profiles in DILs $[C_3(mim)_2](BF_4)_2$, $[C_6(mim)_2](BF_4)_2$, $[C_9(mim)_2](BF_4)_2$ and MIL $[C_3mim][BF_4]$ near negatively (*a*), (*c*) and positively (*b*), (*d*) charged planar carbon electrodes. The number density profile for mono-cation $[C_3mim]^+$ in (*a*), (*b*) was scaled by $\frac{1}{2}$.

5. EDL capacitance

Potential of zero charge. Before presenting EDL capacitance, the PZC is discussed, since PZC was found to be a hallmark of the *C–V* curve [20, 29, 67–69]. For instance, Kornyshev [29] illuminated in a theoretical study that the capacitance reaches a maximum at PZC in a bell-shaped *C–V* curve and a camel-shaped *C–V* curve has a minimum at PZC with two maxima at each side of the PZC. Based on equation (1), we computed the potential distribution from the neutral electrode surface toward the IL $[C_3mim][BF_4]$ bulk, as shown in figure 7(*a*). The PZC is obtained as the potential drop between the electrode

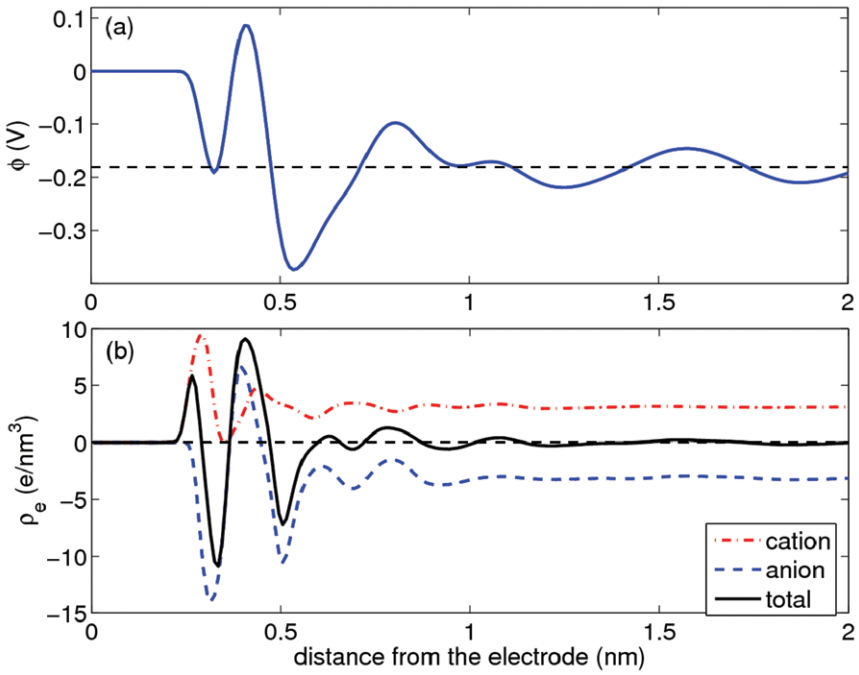

Figure 7. Potential distribution (*a*) and charge density (*b*) profiles in IL $[C_3mim][BF_4]$ near the neutral planar carbon electrode.

surface and bulk ILs, which was found to be 108 mV, 135 mV, 220 mV and 182 mV for $[C_3(mim)_2](BF_4)_2$, $[C_6(mim)_2](BF_4)_2$, $[C_9(mim)_2](BF_4)_2$ and $[C_3mim][BF_4]$, respectively. The positive value of PZC is attributed to the affinity of the cation on the neutral carbon electrode [20, 67], which is evidenced by the fact that the ion–electrode interaction, shown in figure 3, is stronger for the cation $[C_3mim]^+$ than the anion $[BF_4]^-$. It is noteworthy that the affinity of the cation (anion) does not guarantee a positive (negative) PZC. Molecular information, delineated by charge densities from the cation, anion and both cation and anion, can bridge the ion affinity and the PZC value. As shown in figure 7(*b*), the charge closest to the electrode surface is a peak (i.e. positive charge), which originates from the first charge peak contributed by cations. Although there is a negative charge following sequentially, contributed by anions, with a larger magnitude (depth of first valley), the PZC is positive since the positive (negative) charge facilitates positive (negative) PZC and the location of the charge peak (i.e. closer to the surface) has a larger influence on the potential in response to equation (1).

The charge densities from the cation, anion and both cation and anion are shown in figure S2 (stacks.iop.org/J.Phys/26/284106/mmedia) for DILs $[C_3(mim)_2](BF_4)_2$ and $[C_9(mim)_2](BF_4)_2$ near the neutral electrodes. It can be seen that with a very similar first peak of positive charge, the first valley of negative charge becomes deeper for $[C_3(mim)_2](BF_4)_2$ and shallower for $[C_9(mim)_2](BF_4)_2$ in contrast to that for $[C_3mim][BF_4]$, which gives rise to a smaller PZC for $[C_3(mim)_2](BF_4)_2$ and a larger one for $[C_9(mim)_2](BF_4)_2$. Recalling the DIL/MIL structures described in figures 2 and 5, the difference in the first charge valley results from the discrepancy in ion accumulation and orientation, ion–wall interaction and the cation–anion association. That is, the weakest cation–wall interaction (based on interaction potential per unit charge; see figure 3), strongest cation–anion association (figure 4) and the tilted cation (figure 5) in $[C_3(mim)_2](BF_4)_2$ lead to more anions close to the surface as well as more negative charges, while the larger size of the cation and weaker cation–anion association in $[C_9(mim)_2](BF_4)_2$ cause a relatively small amount of negative charges. We also implement this analysis on an IL $[C_2mim][Tf_2N]$, in which the volume of the cation and anion was determined from Molinspiration software (see footnote 3) as 0.1184 nm^3 and 0.1476 nm^3, respectively. As shown in figure S3 (stacks.iop.org/J.Phys/26/284106/mmedia), the anion $[Tf_2N]^-$ has a stronger ion–electrode interaction than the cation $[C_2mim]^+$. Although $[Tf_2N]^-$ has a larger size than $[C_2mim]^+$ and stays further away from the electrode, as shown in figure S4 (stacks.iop.org/J.Phys/26/284106/mmedia), the PZC is found to be −208 mV, because the stronger anion–electrode interaction brings fluorine atoms with highly negative partial charges close to the electrode surface. In short, the PZC is eventually determined by the ion–electrode interaction, ion size/volume and charge delocalization as well as the electrode material and surface topography [20, 29, 67–69].

Differential capacitance. Since the PZC is not zero for all simulation systems explored herein, $V_{EDL} = \phi_{EDL}$–PZC was considered as the potential applied on each EDL for convenience. Figure 8 shows the differential capacitance as a function of applied potential, computed as $C = d\sigma/dV_{EDL}$ for EDLs in DILs $[C_3(mim)_2](BF_4)_2$, $[C_6(mim)_2](BF_4)_2$, $[C_9(mim)_2](BF_4)_2$ and MIL $[C_3mim][BF_4]$ near planar carbon electrodes. It is observed that for DIL $[C_3(mim)_2](BF_4)_2$, the *C*–*V* curve is camel-shaped with a minimum at PZC, whereas quasi-bell-shaped *C*–*V* curves are presented for the other three ILs with a maximum around the PZC. The near-bell-shaped *C*–*V* curve for MIL $[C_3mim][BF_4]$ is in agreement with that of previous studies [63, 70, 71]. The asymmetry of the *C*–*V* curve with the capacitance under positive

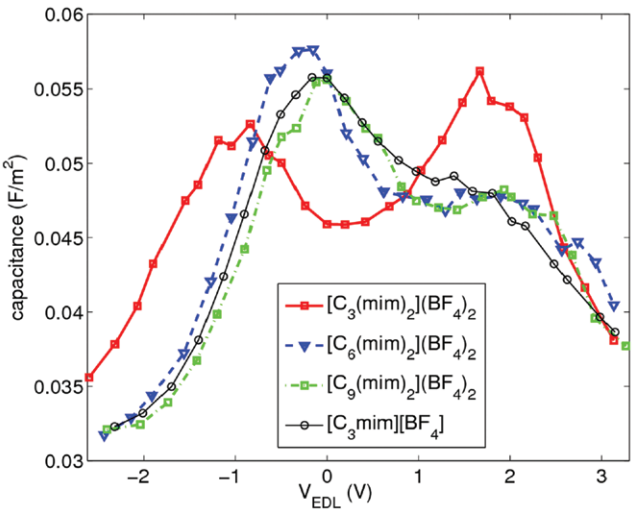

Figure 8. Differential capacitance–electrical potential (*C*–*V*) curves for EDLs in DILs $[C_3(mim)_2](BF_4)_2$, $[C_6(mim)_2](BF_4)_2$, $[C_9(mim)_2](BF_4)_2$ and MIL $[C_3mim][BF_4]$ computed from MD simulation.

potential larger than under negative potential can be attributed to the smaller size of anion $[BF_4]^-$ than the studied cations, which facilitates the formation of a thinner EDL under positive potentials [39, 67, 72–74]. The capacitance for $[C_3(mim)_2](BF_4)_2$ starting to decrease under the potentials of ~−1 and ~1.7 V could be explained by the concept of lattice saturation [75, 76] at large voltages (where the square root of the applied potential, $|V_{EDL}|$, is proportional to the absolute value of surface charge density $|\sigma|$). The relation between $|\sigma|$ and $|V_{EDL}|^{0.5}$ was computed for EDLs near positively and negatively charged electrodes and is shown in figure S5 (stacks.iop.org/J.Phys/26/284106/mmedia). It is observed that lattice saturation occurs at a moderate potential (where $|\sigma| \propto |V_{EDL}|^{0.5}$ holds); i.e. the saturation voltage is about −1.0 V on the negative electrode and around 1.7 V on the positive electrode.

However, the transition of the *C*–*V* curve from camel shape to bell shape as the dication chain length increases and the similarity of the *C*–*V* curve for MIL $[C_3mim][BF_4]$ and DILs $[C_6(mim)_2](BF_4)_2$ and $[C_9(mim)_2](BF_4)_2$ are still not understood. Using a coarse-grained model for ILs, Trulsson *et al* [33] revealed the role of dispersion forces in the *C*–*V* curve of IL and expatiated that both the increase in ion adsorption on the electrode and the decrease in attractive interaction between ions would drive the *C*–*V* curve to clearly change from camel shape to bell shape. In figure 3, the strength of cation–electrode interaction is observed to follow the order: $[C_3(mim)_2]^{2+}$ < $[C_6(mim)_2]^{2+}$ ≈ 2× $[C_3mim]^+$ < $[C_9(mim)_2]^{2+}$ (the potential is −122.2 kJ mol^{-1}, −146.3 kJ mol^{-1}, −171.5 kJ mol^{-1} and −75.8 kJ mol^{-1} for cations $[C_3(mim)_2]^{2+}$, $[C_6(mim)_2]^{2+}$, $[C_9(mim)_2]^{2+}$ and $[C_3mim]^+$, respectively), implying that the increasing ion adsorption on the electrode probably results in the transition of the *C*–*V* curve from camel to bell shape. The size and the ion–electrode interaction potential of monocation $[C_3mim]^+$ is nearly half that of dication $[C_6(mim)_2]^{2+}$, which leads to the similarity of their *C*–*V* curves. To examine the strength trend of the attractive interaction between ions, the ion correlation functions were calculated and are shown in figure 9. It can be seen that the ion–ion correlation functions (also those in figure 4) exhibit a higher first peak in $[C_3(mim)_2](BF_4)_2$ than in the other three ILs. In particular, the anion–anion correlation functions in figure 9(*b*) indicate that the attraction between ions decreases in the order: $[C_3(mim)_2]^{2+}$ > $[C_6(mim)_2]^{2+}$ > $[C_3mim]^+$ > $[C_9(mim)_2]^{2+}$, together with the order of cation–wall adsorption, which accounts for the camel-shaped *C*–*V* curve transitioning to a bell-shaped curve as the chain length increases [33].

5. Conclusions

In summary, we performed MD simulation of ILs with graphene sheets to investigate the interfacial structure and capacitance of EDLs in DILs $[C_3(mim)_2](BF_4)_2$, $[C_6(mim)_2](BF_4)_2$ and $[C_9(mim)_2](BF_4)_2$ as well as MIL $[C_3mim][BF_4]$ near planar carbon electrodes. With a neutral carbon surface, there is a strong adsorbed layer of cations associated with anions near the electrode, which is consistent with previous observations of imidazolium-based monocations adsorbed on the electrode [19, 22, 23]. Interestingly, the adsorbed layer with double peaks is exclusively found for $[C_3(mim)_2](BF_4)_2$ and the cation in the second peak is tilted, unlike that in the first peak parallel to the electrode surface, which can be explained by the weaker cation–wall interaction (based on the interaction potential per unit charge) and stronger cation–anion association in $[C_3(mim)_2](BF_4)_2$ compared with the other three ILs. When electric potential was applied, a distinct peak of counter-ions accumulated on the charged surface, similar to observations in other simulation work using different imidazolium-based MILs [20–22, 63, 65, 66]. However, as electrodes change from neutral to negatively charged, the second peak of dication $[C_3(mim)_2]^{2+}$ is greatly reduced, while those of $[C_6(mim)_2]^{2+}$ and $[C_9(mim)_2]^{2+}$ become non-trivial (figure S6 (stacks.iop.org/J.Phys/26/284106/mmedia)), which suggests different thickness of EDLs in DILs with varying chain lengths and which may be the reason for the transition of the *C*–*V* curve. Meanwhile, the chain of dication becomes more parallel to the surface, while the chain of monocation $[C_3mim]^+$ changes subtly, due to the two-end-linked chain in dications having more constraints than the one-end-free tail in monocation. The value of PZC is associated with the ion affinity, which is eventually determined by the ion–electrode interaction, ion size/volume and charge delocalization as well as the electrode material and surface topography. The differential capacitance of EDLs as a function of applied potential was observed to show a transition from camel shape to bell shape as the dication chain length increases, which is attributed to the enlargement of ion adsorption (per unit charge) on electrode and the decrease of attractive interaction between ions [33]. These *C*–*V* curves for interfaces of DILs and carbon electrodes invite further experimental verification.

It is worthwhile to note that the DIL has a much smaller self-diffusion coefficient than an MIL with a mass comparable cation [64], which would slow down the ion transport during the charge/discharge process. Organic solvents such as

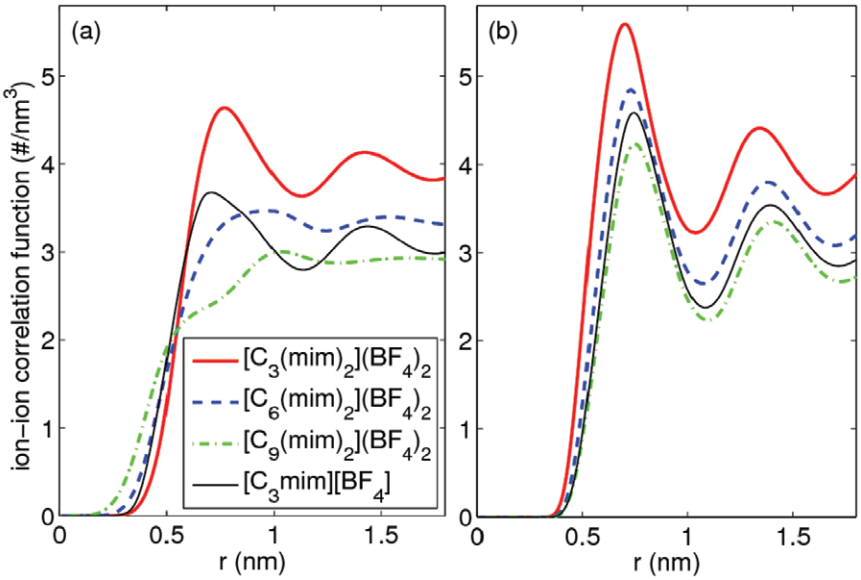

Figure 9. Cation–cation (*a*) and anion–anion (*b*) center-of-mass correlation functions as obtained from MD simulations at 450 K. The values for all dications in (*a*) were scaled by 2 to compare directly with monocation $[C_3mim]^+$.

acetonitrile and propylene carbonate can be added to improve the conductivity and charge/discharge rate [77]. How the presence of an organic solvent as well as the solvation/desolvation of ions influences the EDL structure and capacitance will be investigated in another work.

Acknowledgments

This work was supported by the Fluid Interface Reactions, Structures, and Transport (FIRST) Center, an Energy Frontier Research Center funded by the US Department of Energy, Office of Science, Office of Basic Energy Sciences. We acknowledge the National Energy Research Scientific Computing Center, which is supported by the Office of Science of the US Department of Energy under contract no. DE-AC02-05CH11231. GF appreciates the Palmetto Cluster at Clemson University for providing computer time to complete most simulations performed for this work.

References

[1] Goodenough J B, Abruna H D and Buchanan M V 2007 Basic research needs for electrical energy storage *Report of the Basic Energy Sciences Workshop on Electrical Energy Storage* (*Bethesda, MD, Apr. 2007*)
[2] Tarascon J M and Armand M 2001 Issues and challenges facing rechargeable lithium batteries *Nature* **414** 35967
[3] Miller J R and Simon P 2008 Materials science: electrochemical capacitors for energy management *Science* **321** 6512
[4] Conway B E 1999 *Electrochemical Supercapacitors: Scientific Fundamentals and Technological Applications* (New York: Kluwer/Plenum)
[5] Simon P and Gogotsi Y 2008 Materials for electrochemical capacitors *Nature Mater.* **7** 84554
[6] Wang G, Zhang L and Zhang J 2012 A review of electrode materials for electrochemical supercapacitors *Chem. Soc. Rev.* **41** 797–828
[7] Frackowiak E, Abbas Q and Bguin F 2013 Carbon/carbon supercapacitors **22** 22640
[8] Zhang L L and Zhao X S 2009 Carbon-based materials as supercapacitor electrodes *Chem. Soc. Rev.* **38** 252031
[9] Zhao C, Burrell G, Torriero A A J, Separovic F, Dunlop N F, MacFarlane D R and Bond A M 2008 Electrochemistry of room temperature protic ionic liquids *J. Phys. Chem.* B **112** 692336
[10] Zhou Z-B, Matsumoto H and Tatsumi K 2004 Low-melting, low-viscous, hydrophobic ionic liquids: 1-alkyl(alkyl ether)-3-methylimidazolium perfluoroalkyltrifluoroborate *Chem. Eur. J.* **10** 658191
[11] Zhou Z-B, Matsumoto H and Tatsumi K 2006 Cyclic quaternary ammonium ionic liquids with perfluoroalkyltrifluoroborates: synthesis, characterization, and properties *Chem. Eur. J.* **12** 2196212
[12] Zhou Z-B, Matsumoto H and Tatsumi K 2005 Low-melting, low-viscous, hydrophobic ionic liquids: aliphatic quaternary ammonium salts with perfluoroalkyltrifluoroborates *Chem. Eur. J.* **11** 75266
[13] Ohno H 2005 *Electrochemical Aspects of Ionic Liquids* (New York: Wiley)
[14] Tsai W-Y, Lin R, Murali S, Zhang L, McDonough J K, Ruoff R S, Taberna P-L, Gogotsi Y and Simon P 2013 Outstanding performance of activated graphene based supercapacitors in ionic liquid electrolyte from 50 to 80C *Nano Energy* **2** 40311
[15] Mezger M *et al* 2008 Molecular layering of fluorinated ionic liquids at a charged sapphire (0001) surface *Science* **322** 4248
[16] Pinilla C, Del Pópolo M G, Lynden-Bell R M and Kohanoff J 2005 Structure and dynamics of a confined ionic liquid. Topics of relevance to dye-sensitized solar cells *J. Phys. Chem.* B **109** 179227
[17] Lynden-Bell R M and Del Pópolo M 2006 Simulation of the surface structure of butylmethylimidazolium ionic liquids *Phys. Chem. Chem. Phys.* **8** 94954
[18] Pinilla C, Del Pópolo M G, Kohanoff J and Lynden-Bell R M 2007 Polarization relaxation in an ionic liquid confined between electrified walls *J. Phys. Chem.* B **111** 487784
[19] Wang S, Li S, Cao Z and Yan T 2010 Molecular dynamic simulations of ionic liquids at graphite surface *J. Phys. Chem.* C **114** 9905

[20] Vatamanu J, Borodin O and Smith G D 2010 Molecular insights into the potential and temperature dependences of the differential capacitance of a room-temperature ionic liquid at graphite electrodes *J. Am. Chem. Soc.* **132** 1482533

[21] Vatamanu J, Cao L, Borodin O, Bedrov D and Smith G D 2011 On the influence of surface topography on the electric double layer structure and differential capacitance of graphite/ionic liquid interfaces *J. Phys. Chem. Lett.* **2** 226772

[22] Feng G, Zhang J S and Qiao R 2009 Microstructure and capacitance of the electrical double layers at the interface of ionic liquids and planar electrodes *J. Phys. Chem.* C **113** 454959

[23] Kislenko S A, Samoylov I S and Amirov R H 2009 Molecular dynamics simulation of the electrochemical interface between a graphite surface and the ionic liquid [Bmim][PF_6] *Phys. Chem. Chem. Phys.* **11** 558490

[24] Black J M, Walters D, Labuda A, Feng G, Hillesheim P C, Dai S, Cummings P T, Kalinin S V, Proksch R and Balke N 2013 Bias-dependent molecular-level structure of electrical double layer in ionic liquid on graphite *Nano Lett.* **13** 595460

[25] Perkin S, Crowhurst L, Niedermeyer H, Welton T, Smith A M and Gosvami N N 2011 Self-assembly in the electrical double layer of ionic liquids *Chem. Commun.* **47** 65724

[26] Perkin S 2012 Ionic liquids in confined geometries *Phys. Chem. Chem. Phys* **14** 505262

[27] Smith A M, Lovelock K R J, Gosvami N N, Licence P, Dolan A, Welton T and Perkin S 2013 Monolayer to bilayer structural transition in confined pyrrolidinium-based ionic liquids *J. Phys. Chem. Lett.* **4** 37882

[28] Smith A M, Lovelock K R J and Perkin S 2013 Monolayer and bilayer structures in ionic liquids and their mixtures confined to nano-films *Faraday Discuss.* **167** 279–92

[29] Kornyshev A A 2007 Double-layer in ionic liquids: paradigm change? *J. Phys. Chem.* B **111** 554557

[30] Lockett V, Horne M, Sedev R, Rodopoulos T and Ralston J 2010 Differential capacitance of the double layer at the electrode/ionic liquids interface *Phys. Chem. Chem. Phys.* **12** 12499512

[31] Alam M T, Islam M M, Okajima T and Ohsaka T 2007 Measurements of differential capacitance at mercury/room-temperature ionic liquids interfaces *J. Phys. Chem.* C **111** 1832633

[32] Baldelli S 2008 Surface structure at the ionic liquid–electrified metal interface *Acc. Chem. Res.* **41** 42131

[33] Trulsson M, Algotsson J, Forsman J and Woodward C E 2010 Differential capacitance of room temperature ionic liquids: the role of dispersion forces *J. Phys. Chem. Lett.* **1** 11915

[34] Su Y Z, Yan J W, Li M G, Zhang M and Mao B W 2013 Electric double layer of Au(100)/imidazolium-based ionic liquids interface: effect of cation size *J. Phys. Chem.* C **117** 20512

[35] Alam M T, Masud J, Islam M M, Okajima T and Ohsaka T 2011 Differential capacitance at Au(111) in 1-alkyl-3-methylimidazolium tetrafluoroborate based room-temperature ionic liquids *J. Phys. Chem.* C **115** 19797804

[36] Lockett V, Sedev R, Ralston J, Horne M and Rodopoulos T 2008 Differential capacitance of the electrical double layer in imidazolium-based ionic liquids: influence of potential, cation size, and temperature *J. Phys. Chem.* C **112** 748695

[37] Mayrand-Provencher L, Lin S X, Lazzerini D and Rochefort D 2010 Pyridinium-based protic ionic liquids as electrolytes for Ruo2 electrochemical capacitors *J. Power Sources* **195** 511421

[38] Costa R, Pereira C M and Silva F 2010 Double layer in room temperature ionic liquids: influence of temperature and ionic size on the differential capacitance and electrocapillary curves *Phys. Chem. Chem. Phys.* **12** 1112532

[39] Alam M T, Islam M M, Okajima T and Ohsaka T 2007 Measurements of differential capacitance at mercury/room-temperature ionic liquids interfaces *J. Phys. Chem.* C **111** 1832633

[40] Fedorov M V, Georgi N and Kornyshev A A 2010 Double layer in ionic liquids: the nature of the camel shape of capacitance *Electrochem. Commun.* **12** 2969

[41] Vatamanu J, Borodin O, Bedrov D and Smith G D 2012 Molecular dynamics simulation study of the interfacial structure and differential capacitance of alkylimidazolium bis(trifluoromethanesulfonyl)imide [$C_n$mim][TFSI] ionic liquids at graphite electrodes *J. Phys. Chem.* C **116** 794051

[42] Kurig H, Vestli M, Tonurist K, Janes A and Lust E 2012 Influence of room temperature ionic liquid anion chemical composition and electrical charge delocalization on the supercapacitor properties *J. Electrochem. Soc.* **159** A94451

[43] Feng G, Li S, Presser V and Cummings P T 2013 Molecular insights into carbon supercapacitors based on room-temperature ionic liquids *J. Phys. Chem. Lett.* **4** 336776

[44] Yoshizawa M, Ito-Akita K and Ohno H 2000 Evidence of inter-action between anion and polyether in the bulk *Electrochim. Acta* **45** 161721

[45] Anderson J L, Ding R F, Ellern A and Armstrong D W 2005 Structure and properties of high stability geminal dicationic ionic liquids *J. Am. Chem. Soc.* **127** 593604

[46] Shirota H, Mandai T, Fukazawa H and Kato T 2011 Comparison between dicationic and monocationic ionic liquids: liquid density, thermal properties, surface tension, and shear viscosity *J. Chem. Eng. Data* **56** 24539

[47] Merlet C, Rotenberg B, Madden P A, Taberna P-L, Simon P, Gogotsi Y and Salanne M 2012 On the molecular origin of supercapacitance in nanoporous carbon electrodes *Nature Mater.* **11** 30610

[48] Merlet C, Pan C, Rotenberg B, Madden P A, Daffos B, Taberna P L, Simon P and Salanne M 2013 Highly confined ions store charge more efficiently in supercapacitors *Nature Commun.* **4** 2701

[49] Kondrat S, Georgi N, Fedorov M V and Kornyshev A A 2011 A superionic state in nano-porous double-layer capacitors: insights from Monte Carlo simulations *Phys. Chem. Chem. Phys.* **13** 1135966

[50] Luque N B and Schmickler W 2012 The electric double layer on graphite **71** 825

[51] Rochester C C, Lee A A, Pruessner G and Kornyshev A A 2013 Interionic interactions in conducting nanoconfinement *ChemPhysChem* **14** 41215

[52] Limmer D T, Merlet C, Salanne M, Chandler D, Madden P A, van Roij R and Rotenberg B 2013 Charge fluctuations in nanoscale capacitors *Phys. Rev. Lett.* **111** 106102

[53] Merlet C, Pan C, Rotenberg B, Madden P A, Simon P and Salanne M 2012 Simulating supercapacitors: can we model electrodes as constant charge surfaces? *J. Phys. Chem. Lett.* **4** 2648

[54] Borges R S, Reddy A L M, Rodrigues M-T F, Gullapalli H, Balakrishnan K, Silva G G and Ajayan P M 2013 Supercapacitor operating at 200 degrees Celsius *Sci. Rep.* **3** 2572

[55] Yeganegi S, Soltanabadi A and Farmanzadeh D 2012 Molecular dynamic simulation of dicationic ionic liquids: effects of anions and alkyl chain length on liquid structure and diffusion *J. Phys. Chem.* B **116** 1151726

[56] Lindahl E, Hess B and van der Spoel D 2001 Gromacs 3.0: a package for molecular simulation and trajectory analysis *J. Mol. Model.* **7** 30617

[57] Lopes J N C, Deschamps J and Padua A A H 2004 Modeling ionic liquids using a systematic all-atom force field *J. Phys. Chem.* B **108** 203847

[58] Cornell W D, Cieplak P, Bayly C I, Gould I R, Merz K M, Ferguson D M, Spellmeyer D C, Fox T, Caldwell J W and

Kollman P A 1995 A second generation force field for the simulation of proteins, nucleic acids, and organic molecules *J. Am. Chem. Soc.* **117** 517997

[59] Yeh I C and Berkowitz M L 1999 Ewald summation for systems with slab geometry *J. Phys. Chem.* **111** 315562

[60] Darden T, York D and Pedersen L 1993 Particle mesh Ewald: an *N*log(*N*) method for Ewald sums in large systems *J. Chem. Phys.* **98** 1008992

[61] Hess B, Bekker H, Berendsen H J C and Fraaije J G E M 1997 Lincs: a linear constraint solver for molecular simulations *J. Comput. Chem.* **18** 146372

[62] Allen M P and Tildesley D J 1987 *Computer Simulation of Liquids* (New York: Oxford University Press) p 385

[63] Vatamanu J, Borodin O and Smith G D 2011 Molecular simulations of the electric double layer structure, differential capacitance, and charging kinetics for *N*-methyl-*N*-propylpyrrolidinium bis(fluorosulfonyl)imide at graphite electrodes *J. Phys. Chem.* B **115** 307384

[64] Yeganegi S, Soltanabadi A and Farmanzadeh D 2012 Molecular dynamic simulation of dicationic ionic liquids: effects of anions and alkyl chain length on liquid structure and diffusion *J. Phys. Chem.* B **116** 1151726

[65] Si X, Li S, Wang Y, Ye S and Yan T 2012 Effects of specific adsorption on the differential capacitance of imidazolium-based ionic liquid electrolytes *Chem PhysChem* **13** 16716

[66] Sha M, Zhang F, Wu G, Fang H, Wang C, Chen S, Zhang Y and Hu J 2008 Ordering layers of [Bmim][PF_6] ionic liquid on graphite surfaces: molecular dynamics simulation *J. Chem. Phys.* **128** 134504

[67] Lauw Y, Horne M D, Rodopoulos T, Nelson A and Leermakers F A M 2010 Electrical double-layer capacitance in room temperature ionic liquids: ion-size and specific adsorption effects *J. Phys. Chem.* B **114** 1114954

[68] Islam M M, Alam M T and Ohsaka T 2008 Electrical double-layer structure in ionic liquids: a corroboration of the theoretical model by experimental results *J. Phys. Chem.* C **112** 1656874

[69] Alam M T, Islam M M, Okajima T and Ohsaka T 2008 Capacitance measurements in a series of room-temperature ionic liquids at glassy carbon and gold electrode interfaces *J. Phys. Chem. C* **112** 166008

[70] Fedorov M V and Kornyshev A A 2008 Towards understanding the structure and capacitance of electrical double layer in ionic liquids *Electrochim. Acta* **53** 683540

[71] Feng G, Jiang D E and Cummings P T 2012 Curvature effect on the capacitance of electric double layers at ionic liquid/onion-like carbon interfaces *J. Chem. Theory Comput.* **8** 105863

[72] Islam M M, Alam M T and Ohsaka T 2008 Electrical double-layer structure in ionic liquids: a corroboration of the theoretical model by experimental results *J. Phys. Chem.* C **112** 1656874

[73] Alam M T, Islam M, Okajima T and Ohsaka T 2008 Ionic liquid structure dependent electrical double layer at the mercury interface *J. Phys. Chem.* C **112** 26016

[74] Alam M T, Islam M M, Okajima T and Ohsaka T 2007 Measurements of differential capacitance in room temperature ionic liquid at mercury, glassy carbon and gold electrode interfaces *Electrochem. Commun.* **9** 23704

[75] Georgi N, Kornyshev A A and Fedorov M V 2010 The anatomy of the double layer and capacitance in ionic liquids with anisotropic ions: electrostriction versus lattice saturation *J. Electroanal. Chem.* **649** 2617

[76] Bazant M Z, Storey B D and Kornyshev A A 2011 Double layer in ionic liquids: overscreening versus crowding *Phys. Rev. Lett.* **106** 046102

[77] Cho W J, Yeom C G, Kim B C, Kim K M, Ko J M and Yu K H 2013 Supercapacitive properties of activated carbon electrode in organic electrolytes containing single- and double-cationic liquid salts *Electrochim. Acta* **89** 80713